Powder Technology 479 (2026) 122521

Contents lists available at ScienceDirect

Powder Technology

journal homepage: www.journals.elsevier.com/powder-technology

A unified scaling law for wet powder strength under dynamic loading: Coupling capillary and inertial effects

Lorenzo Schiavo [a,c,*], Erica Franceschinis [b], Andrea C. Santomaso [a]

[a] APTLab - Advanced Particle Technology Laboratory, Department of Industrial Engineering, University of Padova, via Marzolo 9, Padova, 35131, Italy
[b] PharmaTeG – Pharmaceutical Technology Group, Department of Pharmaceutical and Pharmacological Science, University of Padova, via Marzolo 5, Padova, 35131, Italy
[c] INSTM, Consorzio Interuniversitario Nazionale per la Scienza e Tecnologia dei Materiali, Via G. Giusti 9, Firenze, 50121, Italy

HIGHLIGHTS

- Dynamic Ball Indentation characterizes wet powder strength at high strain rates.
- Inertial effects dominate wet powder strength under dynamic loading conditions.
- A unified scaling law couples Capillary and Inertial numbers to predict strength.

GRAPHICAL ABSTRACT

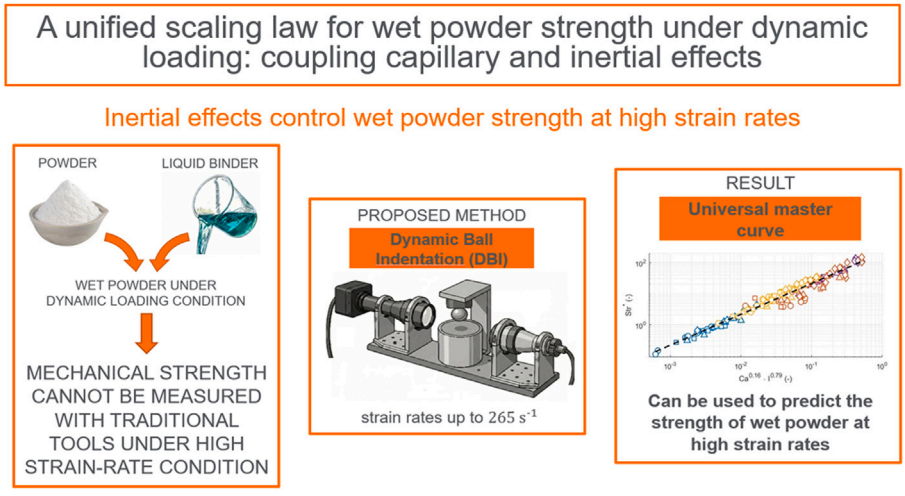

ARTICLE INFO

Keywords:
Dynamic Ball Indentation
Wet powders
Granular rheology
Capillary number
Inertial number
Wet granulation

ABSTRACT

The mechanical strength of wet powders under dynamic loading conditions plays a critical role in numerous industrial and natural processes involving rapid particle rearrangements, including high-shear wet granulation, powder mixing, chute flows and avalanche flows. Despite this importance, existing experimental methods are restricted to quasi-static conditions and fail to capture the rapid deformation regimes characteristic of these processes. This work extends Dynamic Ball Indentation (DBI) to wet granular systems, providing for the first time a method to quantify wet powder strength under the dynamic loading conditions (strain rates $\dot{\gamma}$ = 25–265 s^{-1}) encountered in industrial processes. Experiments covered four granular materials (d_{50} = 5–247 μm) with binders spanning two orders of magnitude in viscosity (η = 1–349 mPa s), at preconsolidation stresses of 1–9 kPa and saturation levels of 5%–75%. Results demonstrate that dependence of dimensionless strength on the Capillary number alone is insufficient to describe wet powder behavior at high strain rates. Instead, a unified scaling law incorporating both viscous-capillary and inertial contributions accurately describes the experimental data: $Str^* = 210.53\ Ca^{0.16}\ I^{0.79}$ (R^2 = 0.96), where Str^* is the dimensionless strength, Ca the

* Corresponding author at: APTLab - Advanced Particle Technology Laboratory, Department of Industrial Engineering, University of Padova, via Marzolo 9, Padova, 35131, Italy.
E-mail address: lorenzo.schiavo@studenti.unipd.it (L. Schiavo).

https://doi.org/10.1016/j.powtec.2026.122521
Received 9 February 2026; Received in revised form 1 April 2026; Accepted 3 April 2026
Available online 20 April 2026

Capillary number, and I the Inertial number. The dominant exponent ($\beta = 0.79$) confirms that inertial effects control wet powder strength under dynamic loading, while viscous dissipation plays a secondary role ($\alpha = 0.16$) These findings establish DBI as an effective characterization tool for dynamic wet powder systems and provide a predictive framework for high-shear granulation process design.

1. Introduction

From industrial granulators operating at high shear rates to natural avalanche flows and powder handling systems, wet granular materials frequently undergo rapid deformation at strain rates exceeding 10^2 s^{-1} [1,2]. Despite the prevalence of such dynamic processes, the mechanical strength of wet powders under rapid loading remains poorly characterized, existing experimental methods typically capture quasi-static behavior and fail to reproduce the momentum-dominated regimes that control particle collisions and flow dynamics. Among industrial applications, wet granulation processes are particularly critical [3]. Granulation is primarily adopted when fine powders are difficult to handle and process, serving multiple purposes: particle size enlargement through agglomeration, reduction of segregation by promoting uniform component distribution, and improvement of powder densification, flowability, and compaction properties [4].

Understanding wet granulation is complex because several competing phenomena occur simultaneously during operation. These have been classified [5,6] as: (1) wetting, nucleation, and binder distribution; (2) consolidation and growth through coalescence and layering; and (3) attrition and breakage. The relative importance of these mechanisms varies both temporally and spatially, making granulation an inherently dynamic rate process [7]. Focusing on granule consolidation – central to this work – the strength of liquid-bound granules is governed by capillary forces, viscous forces, and interparticle friction [8]. Capillary forces provide persistent attractive action that promotes consolidation and resists dilation, while viscous resistance and friction dissipate mechanical energy [8]. For particles with diameters larger than 10 μm, van der Waals and electrostatic forces are typically insignificant compared to liquid bridge forces [9,10].

Powder growth behavior in granulators is not unique [8]. Two main regimes have been identified: steady growth, characterized by rapid coalescence and typically observed with coarse particles and low-viscosity binders; and induction growth, associated with strong, poorly deformable systems where granules initially rebound and growth occurs only after sufficient consolidation [5]. Growth behavior is primarily controlled by deformation during collisions and liquid content [5]. Iveson et al. [11] developed a quantitative framework, to evaluate the growth mechanism based on two dimensionless groups: the Stokes deformation number St_{def} and the maximum pore saturation s_{max}.

The Stokes deformation number:

$$St_{def} = \frac{\rho_g U_c^2}{2Y}, \tag{1}$$

represents the ratio between kinetic energy absorbed during collision (evaluated through the collision velocity U_c and the granule density ρ_g) and the granule yield stress Y.

The maximum pore saturation:

$$s_{max} = \frac{w\rho_s(1-\varepsilon_{min})}{\rho_l \varepsilon_{min}}, \tag{2}$$

characterizes liquid content, where w is the liquid-to-solid ratio, ρ_s and ρ_l solid and liquid densities, and ε_{min} the minimum porosity.

The granulation regime map constructed from these groups identifies distinct behaviors: nucleation (low saturation, low deformation), steady growth (high saturation, high deformation), induction growth (high saturation, low deformation), overwetting(excessive liquid) and crumb formation (excessive deformation). The transition between regimes depends critically on the yield stress Y, whose accurate measurement under representative strain rates is essential for predictive capability.

The critical limitation in predicting granulation behavior lies in measuring the yield stress Y under conditions representative of industrial processes. The yield stress, together with elastic modulus E, governs the impact behavior of powder-binder mixtures and is known to be strain-rate dependent [12]. Conventionally, it is measured using uniaxial or triaxial compression tests; however, these operate at very low strain rates (< 1 s^{-1}) and are therefore not representative of the rapid deformation conditions experienced during granulation [12]. More recently, Iveson measured dynamic yield stress σ_D using a high-speed hydraulic load frame reaching strain rates up to 10 s^{-1}, assuming $Y \approx \sigma_D$[12]. Wet powder compacts with known porosity and liquid content were compressed at constant velocity, and force–displacement data were converted to stress–strain curves, with dynamic yield stress identified as the peak stress. Through dimensional analysis, Iveson identified that the main parameters influencing σ_D are: average particle size (d_p), binder surface tension (γ), binder viscosity (η), solid–liquid contact angle (θ), strain rate ($\dot{\gamma}$), coefficient of internal friction (μ_f), granule packing fraction (Φ), and granule liquid saturation (S):

$$\frac{\sigma_D d_p}{\gamma \cos\theta} = f\left(\frac{\eta\dot{\gamma} d_p}{\gamma\cos\theta}, \mu_f, S, \Phi\right). \tag{3}$$

The left-hand term represents dimensionless strength (Str^*), while the first term on the right-hand side is the Capillary number (Ca), expressing the ratio between viscous and capillary forces. A three-parameter semi-theoretical correlation was formulated:

$$Str^* = k_1 + k_2 Ca^n, \tag{4}$$

with $k_1 = 5.3 \pm 0.4$, $k_2 = 280 \pm 40$, and $n = 0.58 \pm 0.4$.

Despite Iveson's advances, a fundamental gap remains: his method was limited to strain rates up to 10 s^{-1}, while industrial high-shear granulators and other dynamic processes operate at strain rates of 10^2–10^3 s^{-1}—one to two orders of magnitude higher. At these elevated rates, inertial effects may become dominant, potentially invalidating correlations derived from lower-rate experiments. Moreover, conventional methods require substantial sample quantities and lengthy preparation procedures, limiting their practical applicability. The present work addresses this gap by proposing Dynamic Ball Indentation (DBI) as a novel approach to characterize wet powder strength under truly dynamic loading conditions. This technique has recently been successfully applied to dry powder characterization [13–16], demonstrating suitability for investigating dynamic mechanical response of particulate systems. The specific objectives of this study are to:

1. Extend the DBI method to wet granular systems and validate its ability to capture dynamic mechanical response at strain rates representative of industrial processes (10^2–10^3 s^{-1});
2. Investigate the governing dimensionless groups controlling wet powder strength under dynamic loading, including both viscous-capillary (Capillary number) and inertial (Inertial number) contributions;
3. Develop a unified constitutive framework capable of predicting wet powder behavior across wide ranges of material properties, consolidation states, and saturation levels.

2. Materials and methods

The investigated materials are divided in powders and binders. All powder–binder combinations were object of indentation experiment. The selected systems span a wide range of physical properties, including both model (sand-silicone oil) and pharmaceutical (MCC-water) systems. Particle sizes, mechanical bulk behaviors (from elastic MCC to

plastic sand), and powder-binder interactions vary considerably across the dataset. Binders range from Newtonian to shear-thinning fluids, covering roughly two orders of magnitude in viscosity.

2.1. Powders

The powders used in this study were microcrystalline cellulose (MCC, Avicel PH-101, Acef S.p.a, Italy), anhydrous calcium hydrogen phosphate ($CaHPO_4$) with two different particle sizes (Di-Cafos A150 and Di-Cafos A12, Budenheim, Germany), and silica sand (Fontainebleau sand, France).

The surface morphology of the wet powder samples was analyzed by Environmental Scanning Electron Microscopy (ESEM) using a field emission scanning electron microscope (FEI Quanta 200, Philips, Austin, TX, USA) operated at an accelerating voltage of 20 kV. The instrument was equipped with a backscattered electron (BSE) detector and an energy-dispersive X-ray spectroscopy (EDS) system.

ESEM images are shown in Fig. 1. Note that the magnification differs among images because of the different particle size ranges of the powders.

ESEM images highlight the distinct microstructures of the investigated materials. MCC (Fig. 1a) exhibits a fibrous and crystalline structure. This morphology promotes mechanical interlocking between particles and, owing to the presence of surface hydroxyl groups, enables the formation of hydrogen bonds. These interactions result in strong interparticle bonding and high resistance to external stresses [17].

Fig. 1b shows $CaHPO_4$ A150, characterized by triclinic crystals. The crystalline surface limits hydrogen bond formation, leading to relatively weak binder–particle interactions in aqueous systems.

$CaHPO_4$ A12 is obtained by milling the coarser calcium hydrogen phosphate particles. The ESEM image (Fig. 1c) and its magnified inset highlight the fine nature of the powder. The inset reveals particle agglomeration driven by van der Waals and electrostatic forces.

Silica sand (Fig. 1d) exhibits a rigid morphology with irregular, sub-angular to angular particles. Surface features are heterogeneous, with alternating smooth and rough regions. The absence of significant chemical or capillary interactions with binders makes silica sand a suitable reference material for isolating purely mechanical responses. ESEM elemental analysis indicated a surface composition of 98.3% w/w silicon and 1.7% w/w aluminium.

The selection criteria for the powders were based on industrial relevance and on their different responses to wetting. MCC and $CaHPO_4$ are commonly used pharmaceutical excipients: MCC tends to swell upon wetting, whereas $CaHPO_4$ tends to collapse. Silica sand was selected as a non-reactive reference material, as it does not undergo structural changes upon wetting. Furthermore since particle size distribution (PSD) critically affects powder behavior, materials spanning a wide range of particle sizes were chosen to enable a more general assessment of the investigated variables.

2.1.1. Particle size distribution

The volume based particle size distribution was measured by laser light scattering (Malvern Hydro 2000, Malvern, UK) using ethanol as dispersing medium. An obscuration level between 10% and 20% was maintained. Refractive indices of 1.36 were used for ethanol, 1.7 for MCC and $CaHPO_4$ powders, and 1.6 for silica sand.

Prior to measurement, $CaHPO_4$ A12 was sonicated to disrupt agglomerates formed by van der Waals and electrostatic forces, ensuring a representative PSD.

Fig. 2 reports the PSDs, while Table 1 summarizes d_{10}, d_{90}, the median particle diameter d_{50}, the relative span, $S_R = \frac{(d_{90}-d_{10})}{d_{50}}$, and the specific surface area SSA.

$CaHPO_4$ A12 exhibits the smallest median diameter ($d_{50} = 5.0$ μm), followed by MCC ($d_{50} = 54.8$ μm), $CaHPO_4$ A150 ($d_{50} = 167.8$ μm), and silica sand ($d_{50} = 247.1$ μm). $CaHPO_4$ A12 and MCC display broader PSDs ($S_R = 3.9$ and 2.4), whereas $CaHPO_4$ A150 and silica sand show narrower distributions ($S_R = 1.2$ and 0.7). $CaHPO_4$ A12 is the only material exhibiting a bimodal PSD, with peaks at 2.7 μm and 16.3 μm.

Table 1
Particle size distribution parameters and specific surface area of the investigated powders.

Powder	d_{10} (μm)	d_{50} (μm)	d_{90} (μm)	Relative span (–)	SSA (m^2/g)
MCC	14.92	54.8	148.0	2.4	0.209
$CaHPO_4$ A150	87.1	167.8	175.9	1.2	0.0857
$CaHPO_4$ A12	1.7	5.0	21.3	3.9	1.6
Silica Sand	171.9	247.1	352.7	0.7	0.0253

2.2. Binders

The binders used were demineralized water and aqueous solutions of hydroxypropyl methylcellulose (HPMC, nominal viscosity 100,000 mPa s at 2% w/w, Shin-Etsu, JP), prepared at concentrations of 0.75% w/w and 1% w/w. For simplicity, demineralized water is referred to as water, while the HPMC solutions are denoted as HPMC 0.75% and HPMC 1%. HPMC is a cellulose-derived hydrophilic polymer widely used as a pharmaceutical binder [17].

To investigate the effect of a non-polar, high-viscosity liquid, silicone oil (polydimethylsiloxane; density 966.2 kg/m^3; viscosity 339.5 mPa s; Lubrisolve Engineering Solutions Limited, UK) was also employed.

2.2.1. Viscosity

Water and silicone oil behave as Newtonian fluids, with viscosities $\eta_{H_2O} = 1$ mPa s and $\eta_{silicone} = 339.5$ mPa s, respectively. In contrast, aqueous HPMC solutions are non-Newtonian and exhibit shear-thinning behavior, which becomes more pronounced with increasing polymer concentration [18]. At low shear rates, entangled polymer chains increase flow resistance, whereas at high shear rates chain alignment reduces viscosity [17,18].

HPMC concentrations were selected based on viscosity measurements performed with a rheometer (Anton Paar MCR 92, Anton Paar, AT). Concentrations were chosen to ensure a clear deviation from water viscosity across the investigated shear rate range, while remaining industrially relevant.

Each HPMC solution sample was loaded into a 17 cm^3 stainless steel cup. A linear shear rate ramp from 1 s^{-1} to 500 s^{-1} was applied.

The investigated shear rate range was selected based on previous DBI studies [13], which provided a reference. Since the strain rate in DBI experiments cannot be independently imposed, and no significant deviations were expected when varying the powder bed, a comparable range was assumed. A maximum value of 500 s^{-1} was therefore selected to provide a safety margin and ensure full coverage of the DBI shear rates.

Measurements were performed at $T = 25$ °C, consistent with the ambient conditions (19 °C – 23 °C) of the indentation experiments.

Experiment results are shown in Fig. 3, as viscosity against shear rate, each curve represent one concentration of HPMC.

Based on this experiment the concentrations selected for the study were 0.75% w/w, with $\eta_{min} = 25.71$ mPa s and $\eta_{max} = 81.68$ mPa s, and 1% w/w, with $\eta_{min} = 89.42$ mPa s and $\eta_{max} = 312.97$ mPa s.

2.2.2. Surface tension

The surface tension of demineralized water was taken from literature, while that of silicone oil was provided by the manufacturer. The surface tension of the HPMC solutions was determined using the sessile drop method [19]. Drops were deposited on a Teflon surface to minimize liquid–solid interactions and analyzed by image processing.

Due to the sensitivity of the method to drop-shape detection, 10 independent measurements were performed for each HPMC solution. Mean values and standard deviations are reported in Table 2.

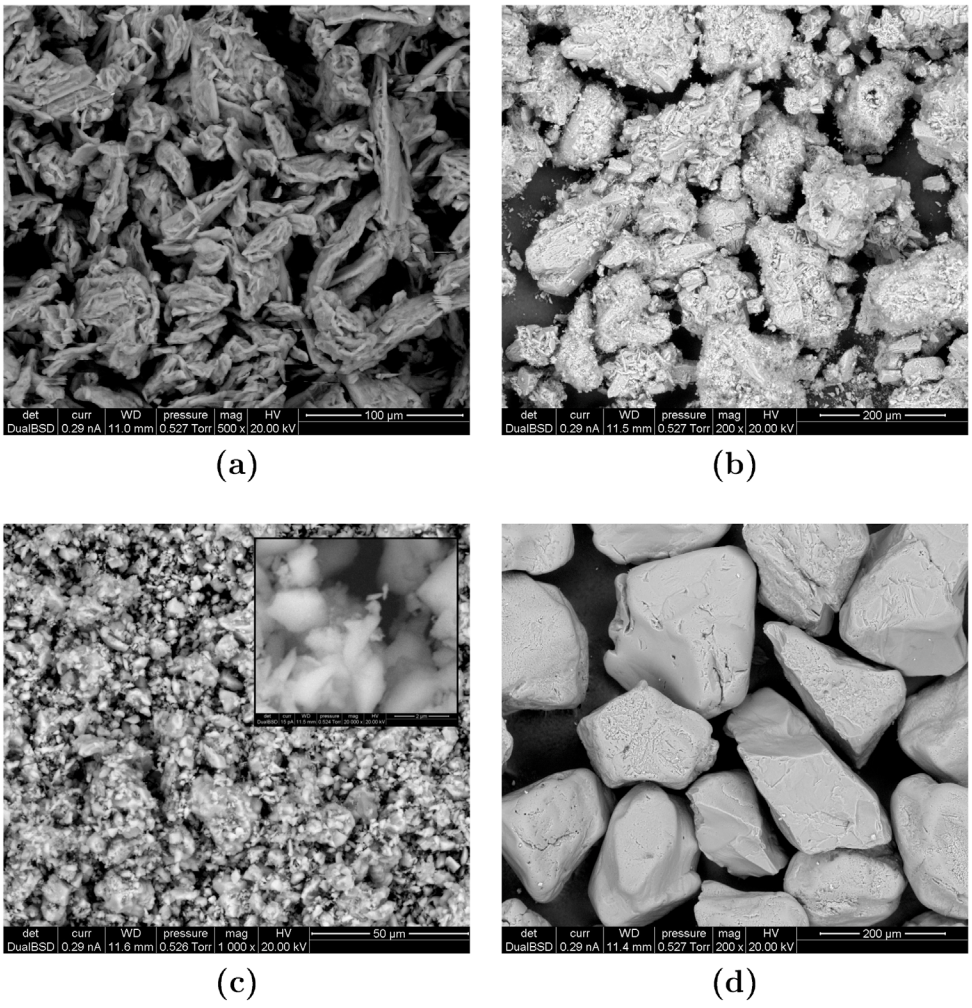

Fig. 1. ESEM images of (a) MCC, (b) $CaHPO_4$ A150, (c) $CaHPO_4$ A12, and (d) silica sand.

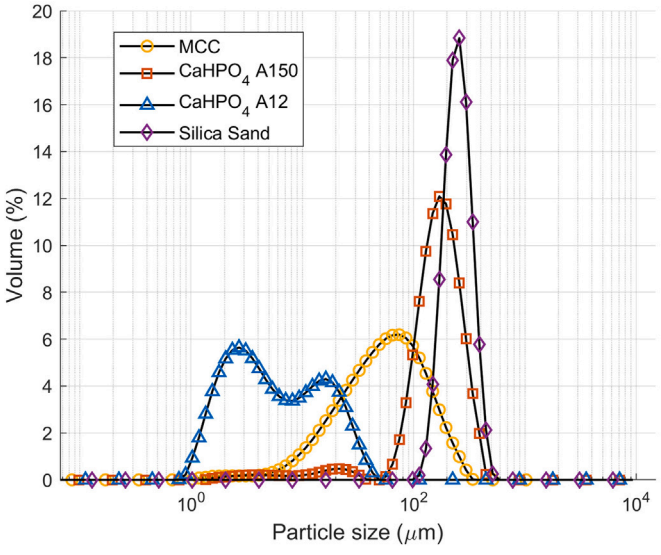

Fig. 2. Volume based particle size distributions of the investigated powders.

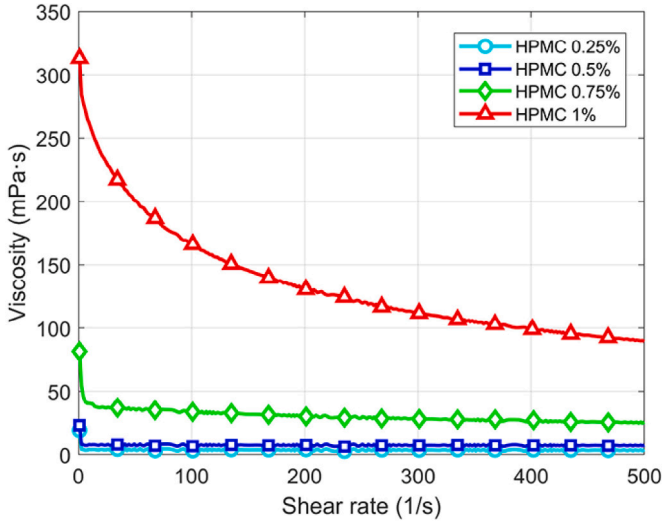

Fig. 3. Viscosity of aqueous HPMC solutions as a function of shear rate for different polymer concentrations. Instrument: Anton Paar MCR 92 rheometer. Applied method: concentric cylinder geometry, linear shear ramp from 1 s^{-1} to 500 s^{-1}, constant temperature at $T = 25$ °C.

Table 2
Surface tension values of the binders used in this study.

Binder	Surface tension [mN/m]	Source/Method
Water (H_2O)	72.8	Literature value at 20 °C, [20]
HPMC solution (0.75% w/w)	48.5 ± 7.3	Sessile drop method
HPMC solution (1.0% w/w)	36.5 ± 11.2	Sessile drop method
Silicone oil	21.1	Manufacturer datasheet

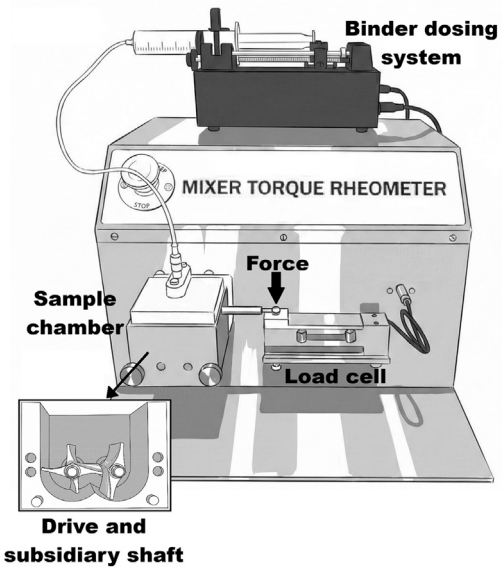

Fig. 4. Schematic of the torque rheometer setup.

2.3. Wet powder characterization

Powder–binder interactions were investigated using a torque rheometer (MTR 3, Caleva Process Instruments, Dorset, UK). Torque rheometry provides a macroscopic measure of the resistance of a powder bed to the rotation of mixing blade at controlled speed. The measured torque reflects the combined effects of interparticle friction, capillary cohesion, and viscous dissipation, providing an indirect quantitative measure of bulk mechanical properties [21].

By progressively increasing the binder content, torque measurements allow for the identification of the transitions between the classical saturation regimes (pendular, funicular, capillary, and droplet), qualitatively illustrated on Fig. 5, [3].

The MTR is specifically designed to monitor changes in cohesiveness and stickiness of powders upon liquid addition. It consists of a mixing chamber equipped with two counter-rotating blades. The chamber is free to rotate around the drive axis, while the torque is transmitted through an arm connected to a calibrated load cell (Fig. 4). This configuration enables the direct measurement of torque variations occurring during the wetting of powders, thereby allowing the study of binder–powder interactions, [3].

Experiments were conducted using the multiple-addition method. Specifically, 12.5 g of MCC or 45 g of $CaHPO_4$ were loaded into the empty chamber and mixed at 150 rpm. Binder was added in steps of 1 mL. After each addition, the wet mass was mixed for 10 s in case of water addition or 20 s for HPMC solutions (higher time to account for their greater viscosity and slower homogenization). Subsequently, the torque value was recorded for 15 s. The total liquid volume added depended on the powder–binder system and was adjusted to reach the overwetting condition.

Fig. 5 shows a typical MTR torque profile where the red dot identify the optimal granulation conditions [22].

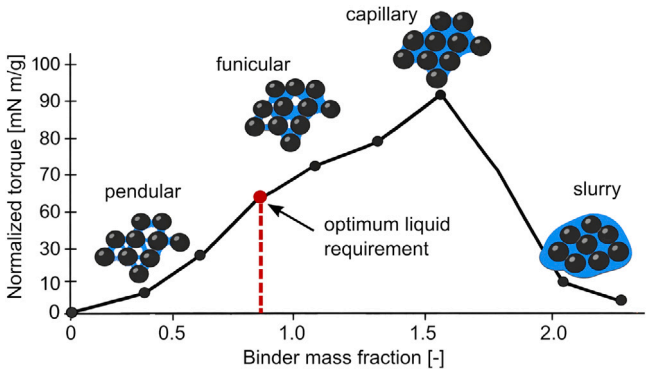

Fig. 5. Typical MTR torque profiles during binder addition [3].

As shown in Fig. 5, the MTR curve typically exhibits a bell-shaped profile: the torque increases to a maximum and then decreases rapidly with the binder addiction. The different regions of this curve correspond to the characteristic saturation regimes of powders. The optimal granulation point is generally located within the funicular regime and corresponds to a mathematical inflection point in the torque curve [3, 22].

In some powder–binder systems (e.g., MCC–water), the torque profile exhibits a clear change in slope, commonly referred to as a "shoulder". This feature is associated with the binder content corresponding to the funicular regime. For instance, in Fig. 7, the MCC–H_2O system (black line, normalized torque measured with MTR) shows a distinct shoulder in the binder mass fraction range $y_b = [0.5, 0.6]$.

In contrast, most powder–binder systems, including the $CaHPO_4$ system investigated in this work, show a smoother torque profile, which obscures this transition. In such cases, the inflection point is determined by calculating the second derivative of the torque signal and identifying the first point where it equals zero [3,22,23].

2.4. Sample preparation and experimental procedure

Wet powder samples were prepared via high-shear mixing to ensure homogeneous binder distribution and to prevent uncontrolled agglomeration. The impeller speed was increased up to 3000 rpm after binder addition to promote rapid liquid redistribution and minimize preferential wetting. Under these conditions, the system is expected to operate in a mechanically dominated regime, ensuring uniform wetting of the powder bed.

The prepared material was then transferred into a cylindrical container and subjected to a progressive uniaxial consolidation protocol. This step was specifically designed to minimize vertical stress gradients and ensure a uniform stress state within the region probed by indentation.

Dynamic ball indentation experiments were performed by releasing a spherical indenter from a fixed height onto the pre-consolidated powder bed. The indenter motion was recorded using high-speed imaging, allowing reconstruction of position, velocity, and acceleration profiles. These were used to derive the force response and dynamic hardness of the material.

A complete and detailed description of sample preparation, consolidation procedure, experimental setup, and data analysis is provided in Appendix A.

3. Results and discussion

3.1. Torque and dynamic hardness comparison

Torque measurements obtained from the rheometer were compared with the dynamic hardness values measured through DBI experiments.

To the authors' knowledge, no studies are currently available in the literature that directly compare these two quantities, even on a qualitative basis, in the context of wet powders. This comparison is motivated by the hypothesis that both techniques probe the same underlying resistance mechanisms – interparticle friction, capillary cohesion, and viscous dissipation – albeit at different length scales and timescales. Establishing a correspondence between these methods would validate DBI as a complementary characterization tool.

From a theoretical perspective, the hardness values obtained by dynamic indentation can be related to the torque measured by the rheometer, since both quantities provide a measure of the material resistance to deformation, although at different length scales and under distinct loading conditions.

In torque rheometry, the measured torque represents the overall resistance of the powder bed to the shear imposed by the rotating blades. This resistance originates from the combined contribution of interparticle friction, cohesive forces due to liquid bridges, and viscous dissipation associated with the binder, [21]. Conversely, the indentation dynamic hardness H_d, defined as the dynamic flow resistance of the indented powder bed surface, [13], is intrinsically a local property. It characterizes the response of a confined volume of material and may therefore not fully capture the bulk behavior. However, provided that the sample preparation ensures sufficient homogeneity and reproducibility, the indented region can reasonably be considered representative of the overall system.

Accordingly, torque rheometry probes the macroscopic response of a relatively large powder volume subjected to continuous shear, whereas indentation experiments probe a localized response under highly concentrated loading conditions.

The characteristic timescales of the two techniques differ significantly. Torque values are averaged over several seconds (15 s in the present experiments) following a homogenization phase. This averaging procedure reduces fluctuations arising from non-uniform resistance during blade–particle interactions, yielding an effective quasi-steady value. In contrast, dynamic ball indentation occurs over a timescale of milliseconds and is inherently non-stationary, allowing fast transient phenomena associated with impact to be captured. Despite these differences in measurement principles, both methods probe the mechanical resistance governed by the same fundamental interactions: friction, capillary forces, and viscous dissipation. Therefore, we expect a qualitative correspondence between torque profiles and dynamic hardness trends as a function of binder content, even if the absolute values and sensitivity differ.

Figs. 6 and 7 compare normalized torque from MTR torque rheometer (black curve) and dynamic hardness from DBI at different consolidation stresses (colored curves) as a function of binder mass fraction $y_b = \frac{w_{binder}}{w_{tot}}$, showing a clear qualitative correspondence. This correspondence is particularly evident in Figs. 6 and 7, where higher torque values systematically correspond to higher indentation hardness. In both cases, peaks are observed at the same binder mass fractions.

It can therefore be stated that the overall shape of the profiles appears to be independent of the measurement timescale. This suggests that the properties measured under quasi-steady conditions using torque rheometry can reflect, at least qualitatively, the mechanical response of the powder bed during rapid impact events. It would nonetheless be of interest to investigate whether the magnitude of the hardness values provides additional insight compared to torque measurements, since DBI more closely reproduces the collisional dynamic conditions encountered in high-shear wet granulators (HSWG). At present, only a qualitative correspondence between the two techniques has been addressed, but this aspect represents a promising direction for future work. Establishing a quantitative conversion factor between torque and dynamic hardness would enable the direct use of DBI measurements for predicting granulator performance.

An important advantage of the hardness method over torque profile evaluation lies in the possibility of assessing material resistance

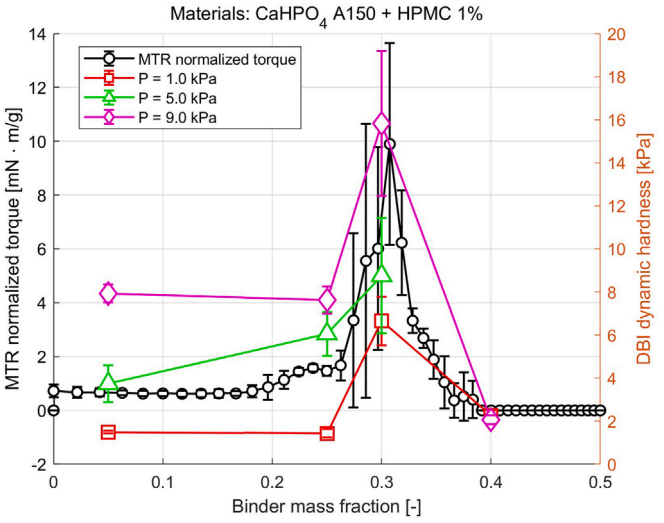

Fig. 6. Comparison between normalized torque from MTR rheometer and dynamic hardness from BDI (at pre-consolidation of 1, 5, and 9 kPa) as a function of binder mass fraction. Materials: $CaHPO_4$ A150 and HPMC 1%.

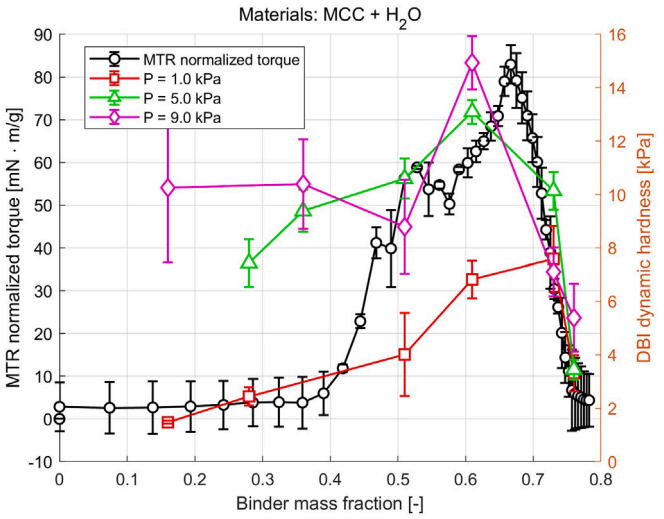

Fig. 7. Comparison between normalized torque from MTR rheometer and dynamic hardness from BDI (at pre-consolidation of 1, 5, and 9 kPa) as a function of binder mass fraction. Materials: MCC and H_2O.

as a function of the preconsolidation stress applied to the powder bed. This information cannot be obtained from torque measurements, since the powder is loaded into the rheometer without any means of controlling compaction. Moreover, the powder is continuously kept in motion by the rotating blades, which prevents the formation of a stable, consolidated bed.

This limitation is overcome by hardness measurements, which allow the resistance of the material to be evaluated as a function of its consolidation state. As shown in Figs. 6 and 7, the peak associated with the capillary regime is preserved even when the consolidation stress is varied.

From a practical standpoint, this capability is valuable for informing granulation process design. The consolidation state of granules within a high-shear mixer evolves dynamically as a result of repeated collisions and compaction events. While the actual stress distribution experienced by individual granules in the granulator remains unknown and spatially heterogeneous, DBI enables the systematic exploration of wet powder strength across a controlled range of preconsolidation stresses. This

approach does not establish a direct correspondence with in-process conditions, but it provides a means of characterizing how consolidation history influences granule mechanical properties, this information can guide the interpretation of granulation behavior and assist in identifying whether a system is likely to exhibit steady growth, induction behavior, or overwetting tendencies [5,7].

In summary, the qualitative correspondence between torque rheometry and dynamic ball indentation validates DBI as a mechanistically meaningful characterization method for wet powders. While both techniques probe the same fundamental resistance mechanisms, DBI offers unique advantages: (i) operation under dynamic, impact-like conditions relevant to high-shear granulation, and (ii) explicit control over consolidation state. These features position DBI as a complementary tool to torque rheometry, capable of bridging the gap between quasi-static powder characterization and dynamic process behavior.

3.2. Dynamic hardness and inertial number

Within the DBI framework, the dependence of the dynamic hardness of dry powders on the Inertial number was previously investigated by Santomaso [13]. In contrast to previous work on DBI, the objective of this study is to explore the applicability of the Inertial number as a descriptor of the mechanical behavior of wet powders, where the presence of a liquid phase introduces additional dissipative and cohesive effects. The Inertial number framework, originally developed for dry granular materials, provides a unified description of flow behavior by characterizing the relative importance of inertial and frictional mechanisms. For wet powders, however, additional forces arise from liquid bridges – specifically, capillary cohesion and viscous dissipation – which are not explicitly captured by the classical Inertial number formulation. The central question addressed in this section is whether the Inertial number can still serve as a meaningful descriptor of wet powder strength, and if not, what modifications or additional dimensionless groups are required.

In the present work, the formulation of the Inertial number introduced by the GDR MiDi group is adopted [24]. This definition was originally proposed to describe the behavior of dry, cohesionless granular materials with particle diameter $d_p > 250$ μm and low-viscosity interstitial fluids (typically gases), where particle interactions are governed predominantly by contact forces [24].

At the grain scale, the Inertial number can be interpreted as the ratio between two characteristic timescales: the timescale associated with the confining stress T_P [24,25],

$$T_P = d_p\sqrt{\frac{\rho_p}{P}}, \tag{5}$$

and the timescale associated with plastic deformation,

$$T_{\dot\gamma} = \frac{1}{\dot\gamma}. \tag{6}$$

Here, $\dot\gamma$ is the strain rate, evaluated as the ratio between the indenter velocity and the penetration depth at the maximum force point:

$$\dot\gamma = \frac{v_{F_{\max}}}{h_{F_{\max}}}. \tag{7}$$

It is worth noting that, in wet granular systems, these are not the only relevant phenomena governing the mechanical response. Additional phenomena are associated with viscous dissipation and capillary interactions, that may become significant depending on the liquid content and binder properties. These effects are not explicitly included in the definition of the Inertial number but will be addressed and discussed in the following sections.

The ratio between the two characteristic timescales introduced above leads to the definition of the Inertial number:

$$I = \dot\gamma\, d_p\sqrt{\frac{\rho_p}{P}}. \tag{8}$$

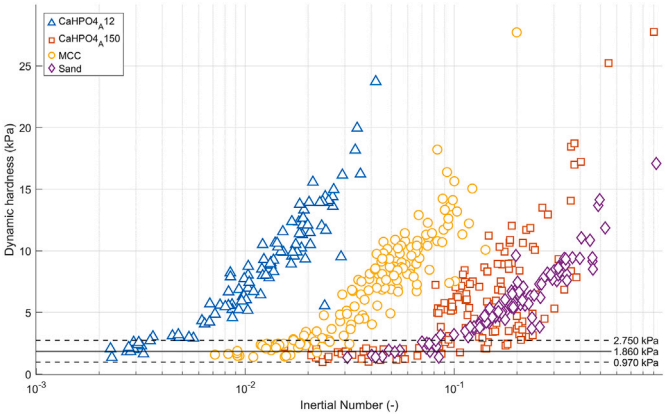

Fig. 8. Dynamic hardness as a function of the Inertial number. Materials: all powder–binder combinations; preconsolidation stress: 1, 5, 9 kPa; binder mass-fraction range: [5–75%].

In the present experiments, indentation occurs very close to the free surface of the powder bed. Under these conditions, before indenter impact, lateral stress transfer can be neglected, and the vertical stress can be reasonably approximated by its hydrostatic contribution over a depth $h = h_{F_{\max}}$ [13,24]. Therefore,

$$P \approx \rho_p g\, h_{F_{\max}}, \tag{9}$$

where $h_{F_{\max}}$ is the indentation depth at the maximum force point, consistently with the definition of dynamic hardness, which is evaluated at the same depth. Substituting this expression into the definition of I yields:

$$I = \dot\gamma d_p\sqrt{\frac{1}{g\, h_{F_{\max}}}}. \tag{10}$$

The particle diameter d_p was taken as the median particle size d_{50} for each powder, as reported in Table 1.

Fig. 8 reports the dynamic hardness H_d as a function of the Inertial number I for all investigated powder–binder combinations, considering three different preconsolidation stresses (1, 5, and 9 kPa) and several binder mass fractions in the range $y_b \in [5–75\%]$.

The distribution of the experimental data across different preconsolidation stresses and binder contents is reported in a supplementary figure in the Supplementary Material.

It is immediately apparent that, when using Eq. (10), the data do not collapse onto a single master curve. Instead, four distinct trends are observed, with each powder type following a separate trajectory. The primary source of this separation is the particle diameter, which spans approximately two orders of magnitude across the investigated powders (from $d_p = 5$ μm for $CaHPO_4$ A12 to $d_p = 247$ μm for sand). This particle-size dependence reveals a fundamental limitation of using the Inertial number alone to describe wet powder behavior. The Inertial number accounts for the ratio of inertial to frictional/confining forces, but it does not explicitly include the contribution of capillary forces, which scale linearly with particle diameter ($F_{cap} \sim \gamma d_p$), or viscous forces, which also depend on particle size through liquid bridge dimensions. As a result, powders with different particle sizes but identical Inertial numbers experience different relative magnitudes of capillary and viscous resistance. This explains why the curves separate systematically by particle size rather than collapsing onto a universal trend.

According to the granular flow framework [24,26], three main flow regimes can be distinguished based on the Inertial number:

- **Quasi-static regime** ($I < 10^{-3}$): deformation is nearly rate-independent and dominated by frictional contacts.

- **Dense or intermediate regime** ($10^{-3} < I < 10^{-1}$): both frictional and inertial mechanisms contribute to the response.
- **Collisional regime** ($I > 10^{-1}$): the behavior is dominated by collisions and inertial dynamics.

Based on this classification, the experiments shown in Fig. 8 fall within the dense regime for $CaHPO_4$ A12 and MCC ($I \approx 10^{-3}$ to 10^{-1}), and extend into the collisional regime for $CaHPO_4$ A150 and sand ($I \approx 10^{-2}$ to 100). However, the observed dependence of H_d on I does not fully align with the classical regime boundaries established for dry granular materials. This deviation is expected, as the regime classifications were developed for systems where only contact forces are significant, whereas wet powders experience additional cohesive and viscous interactions that alter the mechanical response.

All curves exhibit a similar qualitative shape. At relatively low values of I (approximately 7% of the explored Inertial number range for each powder), the dynamic hardness is essentially independent of the Inertial number. This initial plateau region can be classified as quasi-static, in which the system response is rate-independent [24] and governed primarily by capillary cohesion and interparticle friction. The plateau value itself likely reflects the capillary strength contribution, which varies with particle size, liquid content, and surface tension—factors that are not captured by the Inertial number but that govern the baseline resistance in the absence of significant inertial effects. The relatively narrow range of plateau values (0.97–2.75 kPa) compared to the full investigated hardness range (0–30 kPa) suggests that capillary forces provide a modest baseline strength, which is then amplified by inertial effects as I increases.

As the Inertial number increases beyond the plateau, inertial effects progressively influence the flow, and the dynamic hardness becomes rate-dependent. This behavior can be associated with the intermediate or dense regime, where both particle inertia and frictional interactions contribute to the resistance of the powder bed against penetration. In this regime, the nearly linear increase of H_d with I on the log–log plot (approximate slope ~ 0.8–1.0 across all powders) indicates that inertial resistance scales with the characteristic momentum flux associated with particle rearrangements.

No further trend variation is observed that would clearly identify a transition to a fully collisional regime, where particle interactions are dominated by binary collisions rather than sustained contacts. This is most likely due to the absence of experimental points at sufficiently high I values, combined with the inherent limitations of the DBI method in accessing extreme strain rates.

A key limitation of the DBI method is the impossibility of directly prescribing the strain rate, since

$$\dot{\gamma} = \frac{v_{F_{\max}}}{h_{F_{\max}}},$$

and both the indenter velocity and the penetration depth at the maximum force point are determined by the powder response rather than being independently controlled. Increasing the drop height of the indenter would increase the impact velocity, potentially increasing $v_{F_{\max}}$, but it would also lead to a deeper penetration, resulting in only a limited variation of the strain rate. This limitation should be addressed in future work, with the aim of expanding the accessible strain-rate range.

The present results indicate that dynamic hardness can indeed be described as a function of the Inertial number, since the characteristic transition from rate-independent to rate-dependent behavior is consistently observed across all powder-binder combinations. However, using this particular definition of I, the response is not universal and remains dependent on particle size. This systematic shift of the curves with particle diameter is not merely an empirical observation—it has a clear physical origin. Capillary forces, which provide cohesive strength through liquid bridges, scale as $F_{cap} \sim \gamma d_p \cos\theta$. Similarly, viscous forces arising from liquid bridge stretching or compression scale with both viscosity and characteristic dimensions that depend on particle size. Because neither capillary nor viscous contributions are explicitly included in the Inertial number formulation (which was derived for dry, cohesionless systems), their influence appears as a particle-size-dependent offset in the H_d vs. I relationship. This finding motivates the introduction of an additional dimensionless group – the Capillary number – to account for the relative importance of viscous and capillary forces, as explored in the following section.

3.3. Dimensionless force and capillary number

Based on viscous theory and dimensional analysis, Iveson showed that the dynamic strength of a wet powder compact, normalized by the capillary force,

$$Str^* = \frac{Y d_p}{\gamma \cos\theta},$$

depends on the ratio between viscous and capillary forces acting at the single particle–particle level, known as the Capillary number,

$$Ca = \frac{\eta \dot{\gamma} d_p}{\gamma \cos\theta},$$

together with the internal friction coefficient μ_f, the granule saturation S, and the packing fraction Φ [8].

$$\frac{Y d_p}{\gamma \cos\theta} = f\left(\frac{\eta \dot{\gamma} d_p}{\gamma \cos\theta}, \mu_f, S, \Phi\right) \tag{11}$$

In Eq. (11), Y is the dynamic yield stress, d_p the median particle diameter, γ the binder surface tension, θ the contact angle, η the binder viscosity, and $\dot{\gamma}$ the strain rate.

Iveson and co-workers used the peak flow stress σ_{pk} as a proxy for Y, obtained from high-speed compression tests on cylindrical wet powder compacts. Assuming complete wettability ($\cos\theta = 1$), they proposed an explicit dependence of Str^* on Ca alone:

$$Str^* = 5.3 + 280\, Ca^{0.58}. \tag{12}$$

This relation was later extended to include particle aspect ratio and particle size distribution effects [27,28].

In the present work, the dynamic hardness H_d obtained via Dynamic Ball Indentation (DBI) is used as an estimate of Y. This choice is justified by the fact that hardness quantifies the resistance of the powder to irreversible deformation under rapid loading, while Y represents the stress required to activate permanent particle rearrangements. Consequently, both quantities reflect the onset of irreversible deformation. Several studies have linked hardness to the unconfined yield stress through a constraint factor, demonstrating the intrinsic relationship between these two parameters [13,15,16,29,30].

Fig. 9 reports the dimensionless strength as a function of the Capillary number, defined as

$$Str^* = \frac{H_d d_p}{\gamma}, \qquad Ca = \frac{\eta \dot{\gamma} d_p}{\gamma}.$$

The dataset includes three preconsolidation stress levels ($P = 1, 5, 9$ kPa) and binder mass fractions in the range $y_b = 5$–75%. Each data point represents the average of three repetitions. Colors identify the powder, while symbols indicate the binder type. The black line corresponds to Eq. (12) [11], whereas the colored lines represent best fits obtained by grouping experiments performed with the same binder. Each point of the dataset represent the average between three repetitions.

The experimental results deviate significantly from Iveson's reference curve. Instead of collapsing onto a single master curve, the data align along distinct trends associated with the binder type, despite differences in powder material, preconsolidation stress, and binder fraction. This deviation reflects a fundamental difference in experimental conditions: Iveson's correlation was derived from measurements at fixed porosity and saturation, whereas the present dataset explores a much broader parameter space. Since the Capillary number already

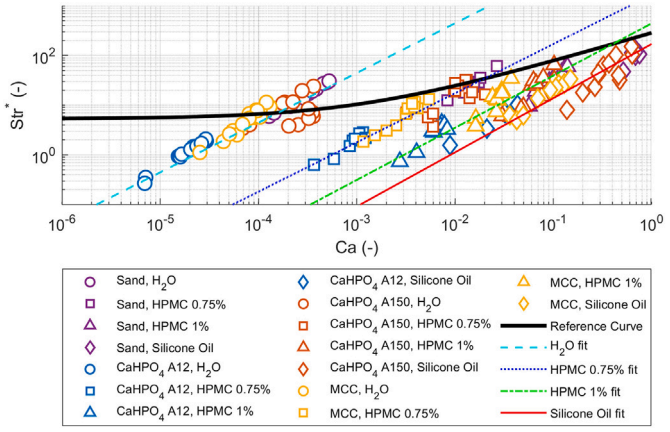

Fig. 9. Dimensionless strength against Capillary number. The black thick line represent Iveson relation, Eq. (12), colored lines represents the fit collecting all the experiments that uses the same binder. Material: all the powder-binder combinations; preconsolidation stress: 1, 5, 9 kPa; binder mass-fraction range: [5-75%].

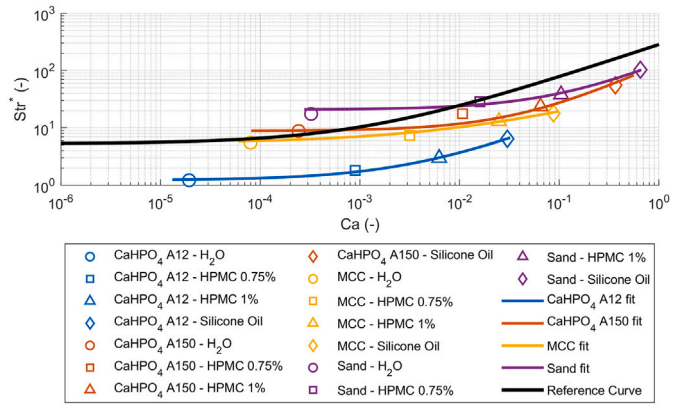

Fig. 10. Dimensionless strength as a function of the Capillary number, with experimental data averaged over different preconsolidation stresses and binder mass fractions. The black thick line represents the Iveson correlation, Eq. (12), while colored lines correspond to fits grouping experiments performed with the same powder.

Table 3
Fitted equation for grouping experiments by binder type.

Binder	Equation	R^2
Water (H_2O)	$Str^* = 44506 \cdot Ca^{0.99}$	0.756
HPMC solution (0.75% w/w)	$Str^* = 1659 \cdot Ca^{0.99}$	0.811
HPMC solution (1.0% w/w)	$Str^* = 442 \cdot Ca^{1.05}$	0.831
Silicone oil	$Str^* = 170 \cdot Ca^{1.09}$	0.834

accounts for η, γ, and $\dot{\gamma}$, and the observed trends successfully group different powders when organized by binder, the separation must arise from the combined effects of consolidation state and liquid saturation—variables that enter the mechanical response but are not explicitly captured by Ca alone.

The fitted equations, all of the form

$$Str^* = k_1\, Ca^n,$$

together with the corresponding R^2 values, are reported in Table 3.

The fitted exponents n are remarkably consistent across binders, with an average value of 1.03 ± 0.04. This near-unity exponent indicates that the dimensionless strength scales approximately linearly with the Capillary number in log–log coordinates, meaning that Str^* is nearly proportional to Ca. The main variation lies in the prefactor k_1, which decreases strongly with increasing binder viscosity and increases with surface tension, ranging from $k_1 \approx 4.5 \times 10^4$ for water to $k_1 = 170$ for silicone oil;

These results indicate that the linear dependence between Str^* and Ca is binder-dependent and that its magnitude is largest for low-viscosity binders, such as water in the present study.

Each binder-dependent trend includes data obtained at different preconsolidation stresses and saturation levels. These variables were not explicitly considered in Iveson's original work [11], which explains why a single universal Str^*–Ca curve does not capture the present experimental results.

This binder-dependent representation of Str^*, although not universal and not sufficient to fully describe the mechanisms governing the response of wet granular materials to applied stresses, is nevertheless potentially valuable. It accounts for variations in consolidation state and liquid saturation without compromising the validity of the single-variable relationship $Str^* = f(Ca)$. Further validation is required, in particular for the binder-dependent prefactor k_1, which appears to be primarily controlled by binder properties. In the absence of a predictive model for k_1, a single indentation test performed with a given binder may be sufficient to determine the corresponding $Str^*(Ca)$ relationship, independently of the powder type, given the approximately linear dependence observed between Str^* and Ca. This approach would enable rapid characterization of wet powder systems without requiring exhaustive experimental campaigns.

A linear dependence of wet powder strength on binder viscosity is consistent with lubrication theory [31]. The viscous force generated during axial stretching or compression of a liquid bridge can be approximated as [8,31]

$$F_v = \frac{3\pi\eta a^2}{2h}\frac{dh}{dt}, \tag{13}$$

where η is the viscosity, a is the harmonic mean particle radius ($1/a = 1/a_1 + 1/a_2$), $2h$ is the interparticle separation, and dh/dt is the relative velocity. This expression shows that viscous resistance scales linearly with viscosity and strain rate (since $\frac{dh}{dt} \sim \dot{\gamma} d_p$), which is precisely the scaling captured by the Capillary number. The dynamic hardness H_d, which quantifies the integrated resistance of many liquid bridges throughout the indented volume, would therefore be expected to scale with Ca when viscous dissipation contributes significantly to the overall mechanical response. The prefactor k_1, in this interpretation, reflects the ratio of capillary to viscous contributions, with lower values of k_1 indicating systems where viscous effects dominate.

Iveson's original experiments [8,12] were conducted under conditions where both porosity and liquid saturation were effectively constant and not systematically varied. In contrast, the present dataset spans a wide range of preconsolidation stresses, which directly control bed porosity [32], as well as several binder mass fractions. These additional degrees of freedom introduce physical effects that were not part of Iveson's experimental framework and may therefore contribute to the observed deviation from his correlation.

To assess whether the discrepancy between the present results and Iveson's model arises from these additional variables, the data were averaged over both preconsolidation stress and binder content. This averaging procedure reduces dispersion associated with porosity and saturation variations, enabling a clearer comparison with the classical Str^*–Ca relationship. Although this operation necessarily modifies the numerical values, it allows the role of Ca to be isolated from the influence of the additional parameters.

The averaged results are shown in Fig. 10.

After removing the variability associated with porosity and saturation through averaging, the data exhibit a markedly improved agreement with the functional form of literature trends. Despite the lack of measurements at low Ca, ($Ca < 10^{-4}$), which limits the ability of

Table 4
Fitted equation.

Powder	Equation	R^2
MCC	$Str^* = 5.371 + 40.752 \cdot Ca^{0.458}$	0.759
$CaHPO_4$ A150	$Str^* = 8.867 + 117.841 \cdot Ca^{0.8}$	0.722
$CaHPO_4$ A12	$Str^* = 1.229 + 57.266 \cdot Ca^{0.680}$	0.759
Sand	$Str^* = 20.796 + 111.751 \cdot Ca^{0.764}$	0.862

fully resolve the intercept term, the averaged curves follow the same analytical form originally proposed by Iveson [11]:

$$Str^* = k_1 + k_2\, Ca^n. \tag{14}$$

The fitted parameters for the different powders are reported in Table 4.

The coefficient of determination R^2 for the averaged fits ranges from 0.72 to 0.86, indicating reasonable agreement but also highlighting residual scatter that cannot be explained by Ca alone. This residual scatter likely reflects the influence of powder-specific properties (e.g., particle shape, surface roughness, interparticle friction) that are not captured by the particle diameter term in Ca.

The ability to recover the characteristic shape of Iveson's correlation confirms that Dynamic Ball Indentation can be used as a suitable tool to identify and quantify the governing mechanisms involved in the mechanical behavior of wet powders.

However, the need to perform averaging to achieve agreement also highlights an important limitation: the Capillary number alone is insufficient to fully describe wet powder strength when consolidation state and liquid saturation vary over a wide range. This finding motivates the development of a more comprehensive constitutive framework that incorporates an additional dimensionless group to account for inertial effects, as explored in the following sections.

3.4. Dimensionless force and inertial number

The analysis presented in Section 3.3 demonstrates that the Capillary number successfully captures the dominant viscous-capillary physics within each binder system, but yields binder-dependent scaling laws characterized by distinct prefactors k_1. This binder dependence indicates that the Capillary number alone cannot provide a universal description of wet powder strength when consolidation state and liquid saturation vary over a wide range and strongly suggests that additional physical mechanisms, not explicitly captured by Ca, contribute to the mechanical response.

To identify these additional mechanisms, we remove the explicit viscosity dependence by analyzing the dimensionless strength as a function of the Inertial number rather than the Capillary number. This approach is motivated by the recognition that, at the high strain rates characteristic of DBI ($\dot{\gamma} \sim$ 25–265 s^{-1}), inertial interactions between particles may play a significant role. The Inertial number,

$$I = \dot{\gamma} d_p \sqrt{\frac{1}{g\, h_{F_{\max}}}},$$

characterizes the relative importance of inertial effects during impact and allows the strength to be studied independently of binder viscosity and surface tension.

The results are shown in Fig. 11. The experiments reveal a clear trend between Str^* and I, with the dimensionless strength increasing with increasing impact inertia and decreasing internal stress.

The observed trend is consistent across different preconsolidation stresses and saturation levels, indicating that the Inertial number effectively captures the influence of these variables on the wet powder strength. This behavior is physically consistent: as I increases (either through higher strain rates or lower confining stress), particle rearrangements become increasingly dominated by inertial momentum transfer rather than quasi-static force balance. Consequently, the

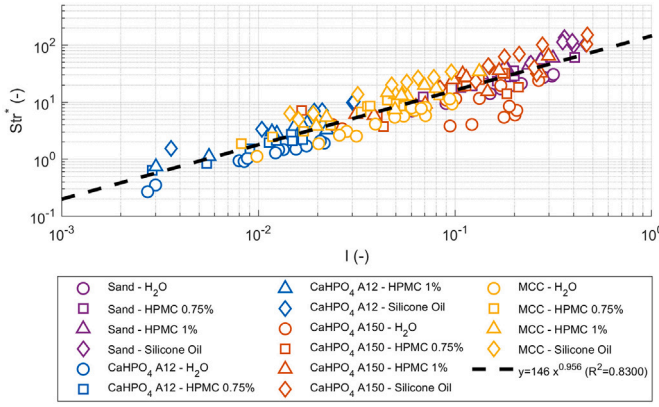

Fig. 11. Dimensionless strength against Inertial number. Material: all the powder-binder combinations; preconsolidation stress: 1, 5, 9 kPa; binder mass-fraction range: [5-75%].

dimensionless strength increases, reflecting the growing contribution of kinetic energy dissipation during particle collisions and the reduced time available for stress relaxation through viscous or frictional mechanisms.

However, the Inertial number alone is insufficient to fully predict the magnitude of Str^*. Data points are shifted vertically depending on the binder used, following the same ordering observed in the Str^*–Ca representation (Fig. 9). Specifically, systems with low-viscosity binders (water) exhibit higher dimensionless strength at a given I, while high-viscosity binders (silicone oil, HPMC solutions) show systematically lower values. This vertical offset reflects the contribution of viscous dissipation, which is not accounted for in the Inertial number. While I characterizes inertial-frictional interactions, it does not capture the rate-dependent viscous resistance that scales with binder viscosity and strain rate—precisely the physics encoded in the Capillary number.

This observation motivates a combined description of wet powder strength based on both Capillary and Inertial numbers.

The Capillary number accounts for viscous-capillary force balance, while the Inertial number captures momentum-dominated deformation and frictional interactions in the dense flow regime. By incorporating both dimensionless groups, we expect to develop a unified scaling law capable of collapsing all experimental data – regardless of powder type, binder properties, consolidation state, or saturation level – onto a single master curve. This constitutive framework, presented in the following section, provides a complete description of wet powder strength under dynamic loading conditions.

3.5. Combined influence of capillary and inertial numbers on dimensionless strength

It is well established in the literature, and confirmed by the present study, that the dimensionless strength (Str^*) depends on the Capillary number (Ca). However, the results presented in Sections 3.3 and 3.4 show that Str^* is also significantly affected by the Inertial number (I), particularly under the high strain-rate conditions typical of Dynamic Ball Indentation.

The objective of this analysis is to provide a unified constitutive description that accounts for the combined influence of capillary–viscous and inertial effects on the strength of wet powders.

Experimental results show that variations in binder viscosity induce a vertical shift in the Str^*–I relationship (Fig. 11), indicating that neither Ca nor I alone is sufficient to describe the observed behavior. Conversely, as demonstrated in Section 3.3, the Str^*–Ca relationship exhibits binder-dependent prefactors, reflecting contributions that are not captured by viscous-capillary scaling alone. This complementary behavior suggests that viscous–capillary effects (quantified by

Ca) and inertial-frictional effects (quantified by I) act as independent but coupled mechanisms governing the mechanical response.

A multiplicative power-law form:

$$Str^* = A\,Ca^{\alpha}\,I^{\beta} \tag{15}$$

would correspond to a linear relationship in logarithmic coordinates:

$$\log(Str^*) = \log(A) + \alpha\log(Ca) + \beta\log(I) \tag{16}$$

and would be consistent with the observed behavior. The exponents α and β quantify the relative contributions of viscous-capillary and inertial mechanisms, respectively, to the overall dimensionless strength.

The exponents α, β and the prefactor A were determined through a global optimization process based on the linearization of the experimental data in logarithmic space. Specifically, the objective function minimized was the Residual Sum of Squares (RSS) of the log-transformed variables:

$$\mathrm{RSS}(A,\alpha,\beta) = \sum_{i=1}^{N}\left[\log(Str_i^*) - \left(\log(A) + \alpha\log(Ca_i) + \beta\log(I_i)\right)\right]^2 \tag{17}$$

where $\log(Str_i^*)$ represents the logarithm of the experimental dimensionless strength measured for the ith data point.

The optimization was performed using a Grid Search algorithm coupled with linear regression. The algorithm explored the parameter space for the exponents within a bounded range ($[-4, 4]$ with a step size of 0.02), calculating the coefficient of determination (R^2) for each combination to identify the global optimum that maximizes the collapse of the experimental data onto the master curve.

The quality of the fit was assessed through the coefficient of determination (R^2), computed in the logarithmic domain as:

$$R^2 = 1 - \frac{SS_{res}}{SS_{tot}} = 1 - \frac{\sum_{i=1}^{N}\left(\log(Str_i^*) - \log(Str_{pred,i}^*)\right)^2}{\sum_{i=1}^{N}\left(\log(Str_i^*) - \overline{\log(Str^*)}\right)^2} \tag{18}$$

where $Str_{pred,i}^*$ is the value predicted by the model, SS_{res} corresponds to the minimized RSS, and SS_{tot} represents the total sum of squares of the deviations between the model predictions and the mean of the experimental logarithmic data ($\overline{\log(Str^*)}$).

The fitting procedure converged to a well-defined set of parameter values with narrow confidence intervals, indicating that the material response is governed by a robust physical scaling. The best-fit parameters, their uncertainties, and the quality of the resulting master curve are presented and discussed in the following section (Section 3.6).

3.6. Proposed constitutive law and physical interpretation

Following the methodology described in Section 3.5, the complete experimental dataset—comprising $N = 185$ experiments spanning four powders ($CaHPO_4$ A12, $CaHPO_4$ A150, MCC, silica sand), four binders (water, HPMC 0.75%, HPMC 1%, silicone oil), three preconsolidation stresses (P = 1, 5, 9 kPa), and binder mass fractions in the range y_b = 5–75%—was fit to the power-law constitutive form.

The optimization procedure converged to the following relationship, where uncertainties represent the 95% confidence intervals derived from the linearized regression:

$$Str^* = (210.53 \pm 24.16)\,Ca^{(0.16\pm0.02)}\,I^{(0.79\pm0.04)} \tag{19}$$

with a coefficient of determination $R^2 = 0.96$.

Fig. 12 reports the dimensionless strength Str^* as a function of the combined variable $Ca^{0.16} \cdot I^{0.79}$ on log–log axes. Experimental data are shown as colored symbols, where the color identifies the powder type and the symbol shape indicates the binder. Despite the wide range of material properties, processing conditions, and saturation levels represented in the dataset, all data collapse onto a single master curve (black dashed line), demonstrating the universality of the proposed scaling law. The scatter around the fitted line is remarkably small, with most

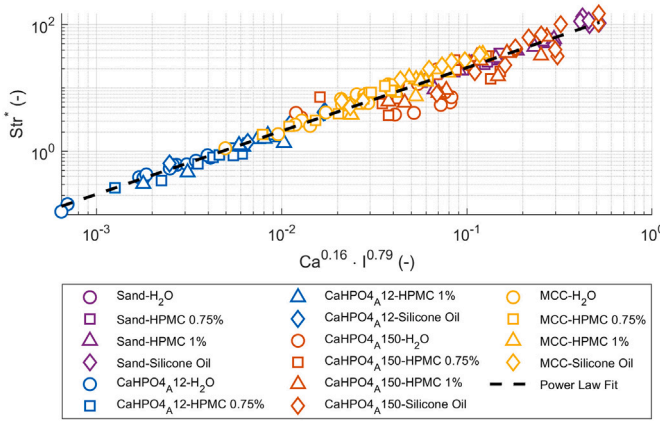

Fig. 12. Dimensionless strength as a function of $Ca^{0.16} \cdot I^{0.79}$. The black dashed line represents the final constitutive law, Eq. (19), with $R^2 = 0.9588$. Material: all powder–binder combinations; preconsolidation stress: 1, 5, 9 kPa; binder mass-fraction range: [5–75%].

data points falling within ±20% of the predicted value. No systematic deviations are observed for any particular powder or binder, confirming that the combination $Ca^{0.16} \cdot I^{0.79}$ successfully captures all relevant physics governing wet powder strength under dynamic loading.

The high coefficient of determination ($R^2 = 0.96$) indicates that 96% of the variance in $\log(Str^*)$ is explained by the model, with only 4% attributed to experimental scatter and unmodeled effects. This level of agreement is very good given the diversity of the dataset and confirms the robustness of the proposed constitutive framework. The residual scatter likely reflects minor contributions from factors not explicitly included in the model, such as particle shape effects, surface roughness variations, and minor differences in packing structure. Nevertheless, the quality of the collapse demonstrates that these secondary effects are negligible compared to the dominant viscous-capillary and inertial mechanisms captured by Ca and I.

The magnitude of the fitted exponents provides direct insight into the governing physical mechanisms:

- **Inertial dominance** ($\beta \approx 0.79$): The exponent associated with the Inertial number is large and close to unity, indicating that penetration resistance is primarily governed by inertial interactions within the granular bed. This is consistent with the high strain rates involved in Dynamic Ball Indentation ($\dot{\gamma} \sim$ 25–265 s^{-1}), where momentum transfer during particle collisions dominates the mechanical response. The near-unity exponent implies an almost linear scaling of the dimensionless strength with the Inertial number, confirming that particle rearrangements occur much faster than viscous stress relaxation.
- **Secondary viscous contribution** ($\alpha \approx 0.16$): The Capillary number enters with a positive but significantly smaller exponent, confirming that viscous dissipation within liquid bridges contributes to the strength but does not control it. This result markedly differs from the rapid-compression scaling proposed by Iveson et al. [8], where $Str^* \propto Ca^{0.58}$. The weaker dependence on Ca in the present work reflects the different deformation regime: DBI operates at higher strain rates and shorter timescales than Iveson's compression tests, leaving less time for viscous stress relaxation.
- **Combined kinematic scaling:** Since both Ca and I depend on the strain rate $\dot{\gamma}$ and particle diameter d_p, the overall scaling of Str^* with these variables can be expressed as

  $$Str^* \sim (\dot{\gamma} d_p)^{\alpha+\beta}.$$

  The sum of the exponents yields $\alpha+\beta \approx 0.95$, indicating an almost linear dependence of the dimensionless strength on the characteristic deformation velocity. This confirms that material resistance

is proportional to the rate at which particles are forced to rearrange, consistent with momentum-controlled behavior typical of dense, rapidly deformed granular systems.

- **Prefactor** ($A \approx 210$): The prefactor A shows relatively little variation across the investigated systems ($A = 210.53 \pm 24.16$), despite substantial differences in material properties. This contrasts with the analysis in Section 3.3, where the prefactor k_1 in the Str^*–Ca relationship varied by more than two orders of magnitude depending on binder properties (from $k_1 \approx 4.5\times10^4$ for water to $k_1 = 170$ for silicone oil). The reduced variability when using the combined $Ca^{\alpha} \cdot I^{\beta}$ framework suggests that the Inertial number term captures additional physics – likely including consolidation-dependent and frictional contributions – that are not explicitly represented by the Capillary number alone. However, given the limited number of material combinations tested (4 powders, 4 binders), broader validation would be necessary to establish whether this consistency extends to other systems. The magnitude of $A \approx 210$ is comparable to Iveson's prefactor of 280 (Eq. (12)), indicating consistency with established wet granulation frameworks.
  It is not yet known whether the prefactor A is universal or depends on microstructural features not explicitly accounted for in the present formulation, such as particle aspect ratio. Further investigation involving a wider range of materials would be required to confirm the generality of this parameter.

In summary, Eq. (19) captures the dual nature of wet powder strength under dynamic loading conditions. The results demonstrate that, in high-speed processes such as dynamic indentation or high-shear granulation, inertial effects dominate over viscous–capillary forces. Neglecting the Inertial number in such processes would therefore lead to a substantial misinterpretation of material behavior.

The proposed model can be recast to retrieve the dynamic hardness as a function of measurable experimental variables. Starting from Eq. (19) and substituting the definitions of Str^*, Ca, and I, we obtain:

$$Str^* = 210\, Ca^{0.16}\, I^{0.79} \rightarrow H_d = 210 \cdot \frac{\dot{\gamma}^{0.95}\, \gamma^{0.84}\, \eta^{0.16}}{d_p^{0.05}\, (g\, h_{F_{\max}})^{0.395}}, \tag{20}$$

where $h_{F_{max}}$ is the penetration depth at maximum force.

This expression reveals several relevant trends. The dynamic hardness is primarily governed by the applied strain rate, showing an almost linear dependence, $H_d \propto \dot{\gamma}^{0.95}$. In contrast, the response exhibits only a weak sensitivity to particle size, $H_d \propto d_p^{0.05}$, indicating limited geometric effects over the investigated diameter range. The contributions associated with binder viscosity and surface tension are comparatively modest, with $H_d \propto \eta^{0.16}$ and $H_d \propto \gamma^{0.84}$. The relatively higher exponent associated with surface tension arises from the definition of Str^* and its propagation through the transformation from Str^* to H_d.

The dynamic hardness obtained from Eq. (20) can be used to estimate the Stokes deformation number:

$$St_{def} = \frac{\rho_c U_c^2}{2H_d}. \tag{21}$$

which, together with the maximum pore saturation s_{max}, enables the use of Iveson's granulation map [7] to assess potential growth behavior in high-shear wet granulation.

4. Conclusions

This work demonstrates that Dynamic Ball Indentation (DBI) provides a robust and physically meaningful framework for characterizing the mechanical strength of wet powders under high strain-rate conditions. By capturing the impact dynamics of a spherical indenter, DBI enables the direct evaluation of dynamic hardness as a proxy for the stress required to trigger irreversible particle rearrangements, bridging the gap between quasi-static characterization methods and the dynamic conditions encountered in high-shear wet granulation.

Through systematic investigation of four powders ($CaHPO_4$ A12, $CaHPO_4$ A150, MCC, silica sand), four binders (water, HPMC 0.75%, HPMC 1%, silicone oil), three preconsolidation stresses (1, 5, 9 kPa), and binder mass fractions ranging from 5% to 75%, a comprehensive dataset spanning a wide range of material properties and processing conditions was assembled. A qualitative correspondence between torque rheometry and dynamic hardness was established across varying binder contents, confirming that DBI captures the same underlying physical mechanisms governing wet powder resistance. Unlike torque measurements, however, DBI allows the explicit investigation of the role of preconsolidation stress, providing access to information that is otherwise inaccessible through conventional rheometric techniques.

The classical dimensionless description of wet powder strength based solely on the Capillary number was found to be insufficient to describe the present experimental dataset. While the characteristic Str^*–Ca dependence proposed in the literature can be recovered when porosity and saturation effects are averaged out, the full dataset exhibits binder-dependent prefactors (k_1) that vary by more than two orders of magnitude—from $k_1 \approx 4.5 \times 10^4$ for water to $k_1 = 170$ for silicone oil. This systematic variation indicates that the Capillary number alone cannot account for all relevant physics when consolidation state and liquid saturation vary over wide ranges. Similarly, analysis of dimensionless strength as a function of the Inertial number alone revealed vertical shifts depending on binder viscosity, confirming that neither Ca nor I individually provides a complete description. These observations highlighted the critical role of inertia, which is not accounted for in traditional scaling approaches, and the need for a combined framework that accounts for both viscous-capillary and inertial-frictional mechanisms.

A constitutive law based on the multiplicative coupling of the Capillary and Inertial numbers successfully collapsed all experimental data onto a single master curve. Through a global optimization process based on the linearization of the experimental data in logarithmic space, the following relationship was established:

$$Str^* = (210.53 \pm 24.16)\, Ca^{(0.16\pm0.02)}\, I^{(0.79\pm0.04)}$$

with a coefficient of determination $R^2 = 0.96$. This scaling law reveals that wet powder strength under dynamic loading is strongly controlled by inertial interactions ($\beta \approx 0.79$), with viscous dissipation acting as a secondary, yet non-negligible, contribution ($\alpha \approx 0.16$). The sum $\alpha + \beta \approx 0.95$ indicates an almost linear dependence of dimensionless strength on the characteristic deformation velocity ($\dot{\gamma} d_p$), consistent with the importance of inertial effects at the high strain rates characteristic of DBI.

The proposed constitutive framework extends classical wet granulation theory to dynamic regimes and provides a quantitative link between dynamic indentation measurements and granulation growth maps. By enabling the estimation of the Stokes deformation number under realistic process conditions, this approach offers a new pathway for predicting granulation regimes in high-shear wet granulators.

Overall, this study establishes Dynamic Ball Indentation as a powerful experimental tool for the dynamic characterization of wet powders and introduces a unified scaling framework capable of capturing the coupled effects of viscosity, capillarity, inertia, saturation and consolidation. The results demonstrate that:

- Inertial effects dominate wet powder strength under high strain-rate conditions;
- Viscous-capillary contributions, while secondary, remain significant;
- A unified constitutive law can be achieved by combining dimensionless groups that separately characterize viscous-capillary (Ca) and inertial-frictional (I) mechanisms.

The results open new perspectives for the rational design, control, and scale-up of wet granulation processes operating under highly dynamic conditions.

Several limitations should be acknowledged, and opportunities for future research identified. First, similarly to other works in literature [8], the present study assumes complete wettability (contact angle $\theta = 0$), which may not hold for all powder-binder systems. Systems characterized by partial wettability (e.g., silicone oil) are nevertheless well captured by the proposed scaling framework, even without explicitly accounting for the contact angle. Future work may consider incorporating the contact angle into the dimensionless groups, although this is expected to mainly induce a shift in the data, with limited improvement in the overall predictive capability. Second, while the dataset spans a wide range of particle sizes (5–247 μm), binder viscosities (1–340 mPa s), and surface tensions (21–73 mN/m), further validation with additional material combinations – particularly those exhibiting strong non-Newtonian behavior or time-dependent rheology – would strengthen the generality of the proposed framework. Third, direct measurement of interparticle friction coefficients under wet conditions would enable more explicit testing of the hypothesis that binder-dependent friction is captured by the Inertial number term.

CRediT authorship contribution statement

Lorenzo Schiavo: Writing – original draft, Software, Formal analysis, Data curation. **Erica Franceschinis:** Visualization, Resources. **Andrea C. Santomaso:** Writing – review & editing, Validation, Supervision, Resources, Project administration.

Declaration of competing interest

The authors declare that they have no known competing financial interests or personal relationships that could have appeared to influence the work reported in this paper.

Appendix A. Detailed experimental procedure

A.1. Sample preparation and powder bed consolidation

Before each indentation test, wet powder bed was prepared following a standardized protocol.

The required amount of powder was weighed and transferred into a high shear mixer (Eirich 1L, Germany), the latter was used to obtain an homogeneous mixture and to avoid the auto-agglomeration, revealed critical for $CaHPO_4$.

The binder was then measured to achieve the target powder-to-liquid ratio.

The liquid binder was introduced into the high shear mixer through a pipe directed toward the center of the chamber. Binder addition was performed at low impeller speed (300 rpm) to avoid powder adhesion to the walls. After dosing, the impeller speed was increased to 3000 rpm for 30–50 s until uniform wetting was achieved.

Uniform wetting was qualitatively assessed by visual inspection of the mixture, ensuring the absence of visible dry regions or binder-rich agglomerates.

Under these conditions, shear-induced demixing is not expected, as the formation of capillary bridges upon binder addition promotes particle cohesion and limits segregation. However, preferential wetting may occur during the initial stages of liquid addition due to the localized injection of the binder and, in some cases, its high viscosity.

The high impeller speed conditions were imposed during and after dosing, in order to mitigate the preferential wetting ensuring rapid redistribution of the liquid phase. According to the nucleation regime map proposed by Hapgood et al. [33], the present operating conditions are expected to fall within a mechanically dominated regime, where mixing-induced dispersion prevails over localized wetting phenomena, leading to an homogeneous distribution of the binder.

Once the wet powder bed was ready, samples were prepared and tested within approximately 5 min to limit binder evaporation, particularly for water and HPMC-based formulations.

Sample preparation followed the protocol described by Santomaso [13]. The wet powder was first poured into a cylindrical Teflon container (volume 150 mL; diameter 60 mm; height 54 mm). Teflon was selected to reduce wall effects during indentation, as recommended by Zafar et al. [34]. Deposition was performed by pluviation to promote homogeneous filling [34,35]: the wet powder was gently passed through a mesh positioned 1 cm above the container rim. Excess powder was removed by leveling the surface.

After filling, uniaxial consolidation stresses of 1, 5, or 9 kPa were applied to the powder using a Teflon piston. The load was maintained for 40 s to reduce elastic recovery by allowing internal stresses to relax. The load was then removed and additional wet powder was added compensating for the volume reduction caused by the compression. The sequence of compression, leveling, and refilling was repeated until no further settling occurred and the final free surface was aligned with the container upper rim.

This progressive consolidation procedure was designed to minimize vertical stress gradients in the powder bed. Without this approach, a single top-loading step would result in higher consolidation at the surface and progressively lower stress with depth. The iterative sequence ensured that the entire region accessed by ball indentation – extending approximately 2-3 ball diameters (≈ 16–24 mm) below the surface [34] – reached uniform consolidation at the target stress level. Because the material was wet, minor surface irregularities could appear due to particle adhesion to the leveling tool; however, their effect was negligible.

A.2. Indentation experiment

Indentation tests were performed using a chrome steel sphere with diameter $D_b = 8$ mm. The sphere was held by an electromagnet at a fixed distance $h_{fall} + D_b = 14.6$ mm above the powder bed, where h_{fall} is the sphere free fall height.

The impact was recorded using an high-speed camera (iSpeed-220, IXCAMERAS LTD) at 10,500 fps, the camera was equipped with a telecentric lens (TC3MHR036-C, Opto Engineering, IT) in combination with a telecentric back-light (LTCLHP036-G, Opto Engineering, IT).

The additional optical components were required to improve the accuracy and reliability of the measurements. Their main role was to eliminate perspective errors caused by changes in the relative distance between the indenter and the camera (e.g. when the ball is closer to the camera it appears larger, while at a greater distance it appears smaller). This effect leads to errors in the pixel-to-length conversion. By removing perspective distortion, the apparent size of the sphere remains constant, allowing a unique and fixed conversion factor to be defined, since the sphere diameter is known.

The camera–light system was mounted on a rigid support to maintain precise alignment between the telecentric light and the camera.

A schematic of the setup is shown in Fig. A.13.

The indentation experiment proceed as follows, the spherical indenter is attached to the electromagnet, activated by an external switch. The pre-consolidated powder bed is placed between the optic lens and the back-light, under the indenter.

The recording is started and the electromagnet switch is turned into off position.

In this way the indenter falls and penetrates the powder bed.

The indentation lasted a few milliseconds, while the entire procedure from the bed placement to the bed removal required less than 20 s, highlighting the rapidity of the method.

After the indentation the sphere is carefully removed using a magnet to keep the bed intact and cleaned to remove powder traces remained on the surface.

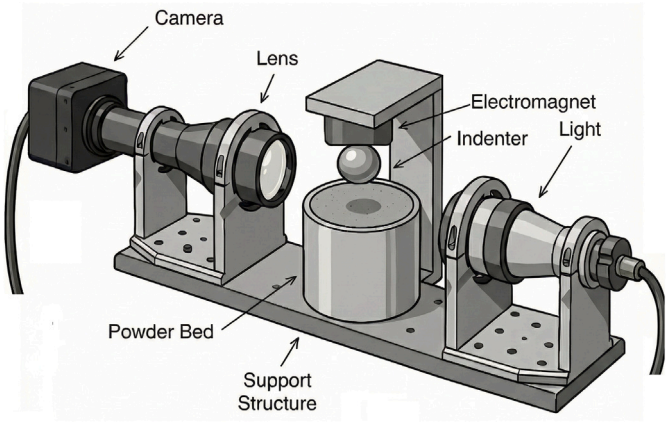

Fig. A.13. Dynamic ball indentation setup; sphere and powder bed not to scale.

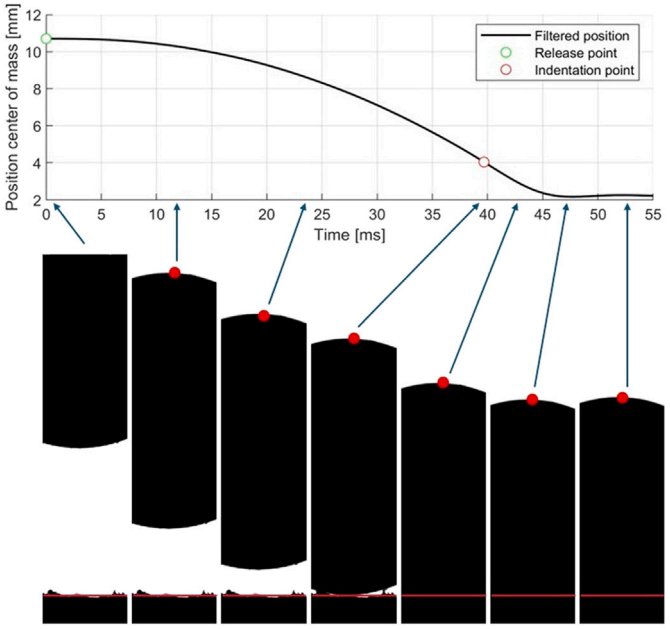

Fig. A.14. Sequence of selected frames. Each frame is connected to the corresponding time instant on the plot above, which represents the trajectory of the indenter. The red markers identify the detected position of the sphere used for trajectory tracking, while the red line indicates the bed surface. The sequence illustrates the progressive penetration of the indenter and forms the basis for the extraction of kinematic quantities.

Multiple indentations were performed on each bed, respecting a minimum spacing of $1.5D_b$ between impacts and from the walls [34]. The large area available to indentation allowed 3 impacts per sample.

Fig. A.14 shows a sequence of selected frames from a dynamic indentation experiment. Each frame is connected by an arrow to the corresponding time instant along the indenter trajectory during the experiment. The region of interest (ROI), captured by the camera does not include the whole sphere, but just the central portion of it. The upper red point of the sphere was tracked to reconstruct its trajectory. The red line represent the bed position and was automatically detected on the first frame using a threshold criterion and applied to all subsequent frames, since the sample remains stationary during the indentation.

Recording only the central portion of the sphere reduces computational load and enables higher frame rates (up to 10,500 fps vs. 7000 fps in previous DBI studies [13]), allowing better temporal resolution of particle rearrangement dynamics during indentation.

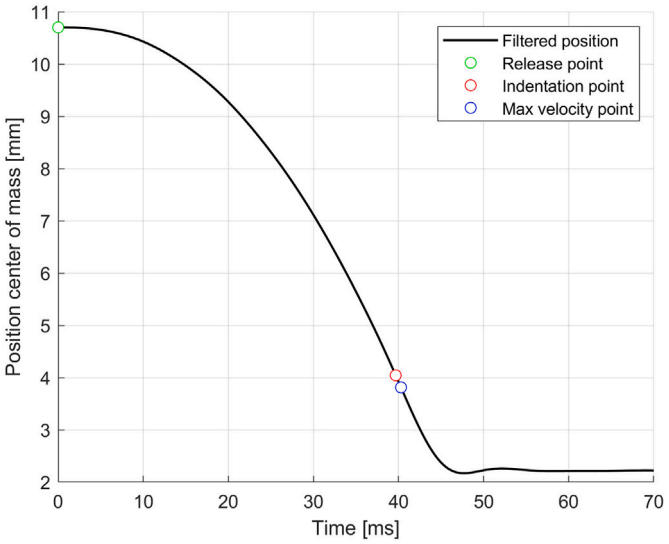

Fig. A.15. Example of indenter center of mass position profile in function of time (from release to rest). Material: MCC; preconsolidation stress: 5 kPa; indenter diameter: 8 mm.

The possibility of increasing the captured fps has the potential benefit of getting closer to the characteristic time of the rearrangement phenomena that the powder undergoes when indented.

A.3. Data analysis

The frame analysis followed the sequential procedure described by Santomaso for DBI [13]. Frames were processed in chronological order, and image segmentation techniques were applied to identify the upper point of the indenter in each frame. The reference zero level for the position measurement was defined as the powder bed surface. The detected sphere upper point was then tracked frame by frame and converted into a continuous trajectory. By subtracting the sphere radius from the coordinate of the upper point, the trajectory of the indenter center of mass was obtained.

The resulting trajectories were smoothed using a digital filter specifically designed to avoid phase shifts or time delays in the processed signals. Velocity and acceleration profiles were subsequently calculated by time differentiation of the smoothed position data. An example of the resulting position and velocity profiles are shown in Figs. A.15 and A.16; these data refer to MCC.

Forces acting on the indenter were calculated using Newton's second law. The gravitational contribution was subtracted in order to isolate the mechanical response of the powder bed and remove the effect of the indenter weight:

$$F_{\text{net}} = [a(t) - g]\, m. \tag{22}$$

The dynamic hardness was calculated using the formulation proposed by Santomaso [13]:

$$H_d = \frac{F_{\max}}{A_{\text{cap}}}, \tag{23}$$

where the contact cap area was evaluated at the point corresponding to the maximum force:

$$A_{\text{cap}} = \pi D_b\, h_{F_{\max}}. \tag{24}$$

where $h_{F_{\max}}$ was the ball penetration depth at the maximum force instant.

All the data processing steps described above were implemented using a dedicated MATLAB® code.

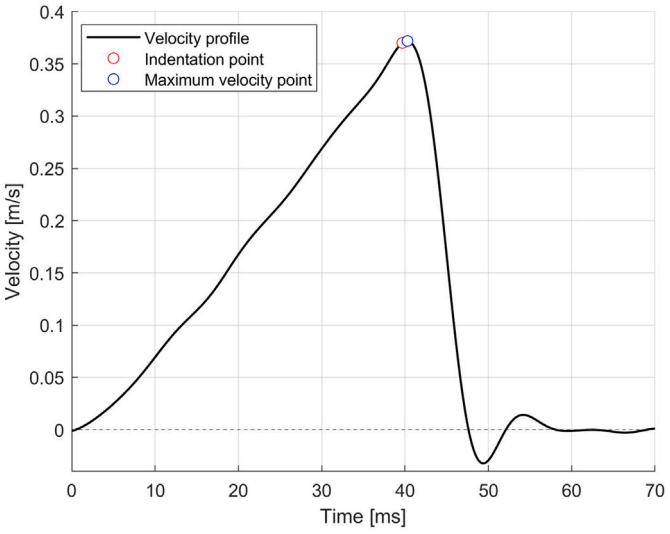

Fig. A.16. Example of indenter center of mass velocity profile in function of time (from release to rest). Material: MCC; preconsolidation stress: 5 kPa; indenter diameter: 8 mm.

Appendix B. Declaration of generative AI and AI-assisted technologies in the manuscript preparation process

During the preparation of this work the authors used ChatGPT-5.2 in order to improve language and readability. After using this tool/service, the authors reviewed and edited the content as needed and take full responsibility for the content of the published article.

Nomenclature

A	Scaling law, pre-factor
a	Acceleration
A_{cap}	Cap Area
Ca	Capillary number
D_b	Ball indenter diameter
d_p	Powder diameter
ϵ_{min}	Minimum granule porosity
F_{net}	Net force
F_v	Viscous force
g	Gravitational acceleration
H_d	Dynamic hardness
h_{fall}	Indenter free fall height
$h_{F_{\max}}$	Penetration at maximum force instant
I	Inertial number
m	Mass
μ_f	Internal friction coefficient
η	Viscosity
P	Pressure
π	constant $\pi = 3.14$
Φ	Packing fraction
ρ_g	Granule density
ρ_l	Liquid density
ρ_s	Solid density
R^2	Coefficient of determination
s_{max}	Maximum pore saturation
S	Liquid saturation
S_R	Relative span
SSA	Specific surface area
St_{def}	Stokes deformation number
Str^*	Dimensionless strength
σ_D	Iveson's dynamic yield stress
T	Temperature
t	Time
U_c	Collision velocity
$v_{F_{max}}$	Indenter velocity in the maximum force instant
$v_{F_{max}}$	Velocity at maximum force instant
Y	Yield stress
y_b	Binder mass fraction
α	Scaling law, Ca power law coefficient
β	Scaling law, I power law coefficient
$\dot{\gamma}$	Shear rate
γ	Surface tension
θ	Solid–liquid contact angle

Appendix C. Supplementary data

Supplementary material related to this article can be found online at https://doi.org/10.1016/j.powtec.2026.122521.

Data availability

Data will be made available on request.

References

[1] Riccardo Artoni, et al., Collapse of quasi-two-dimensional wet granular columns, Phys. Rev. E—Stat Nonlinear Soft Matter Phys. 87 (3) (2013) 032205.
[2] Andrea Claudio Santomaso, Silvia Volpato, Fabio Gabrieli, Collapse and runout of granular columns in pendular state, Phys. Fluids 30 (6) (2018).
[3] Andrea C. Santomaso, et al., Sugars with different thickening power in high shear granulation, Powder Technol. 317 (2017) 391–399.
[4] Ana Rita Alves, et al., A review on the scale-up of high-shear wet granulation processes and the impact of process parameters, Particuology 92 (2024) 180–195.
[5] Jim Litster, Bryan Ennis, The Science and Engineering of Granulation Processes, Vol. 15, Springer Science & Business Media, 2004.
[6] James Iveson, Lister, et al., Nucleation, growth and breakage phenomena in agitated wet granulation processes: a review, Powder Technol. 117 (2001).
[7] Simon M. Iveson, et al., Nucleation, growth and breakage phenomena in agitated wet granulation processes: a review, Powder Technol. 117 (1–2) (2001) 3–39.
[8] Simon M. Iveson, Jai A. Beathe, Neil W. Page, The dynamic strength of partially saturated powder compacts: the effect of liquid properties, Powder Technol. 127 (2) (2002) 149–161.
[9] H Rumpf, The strength of granules and agglomerates, Agglomeration (1962) 379–418.
[10] Ajit S. Narang, Sherif I.F. Badawy (Eds.), Handbook of Pharmaceutical Wet Granulation: Theory and Practice in a Quality By Design Paradigm, Academic Press, 2018.
[11] Simon M. Iveson, et al., Growth regime map for liquid-bound granules: further development and experimental validation, Powder Technol. 117 (1–2) (2001) 83–97.
[12] Simon M. Iveson, Neil W. Page, Dynamic strength of liquid-bound granular materials: the effect of particle size and shape, Powder Technol. 152 (1–3) (2005) 79–89.
[13] Andrea C. Santomaso, Dynamic ball indentation: advancing powder flowability characterization through complete impact dynamics analysis, Adv. Powder Technol. 36 (7) (2025) 104914.
[14] Umair Zafar, et al., Effect of strain rate on powder flow behaviour using ball indentation method, Powder Technol. 380 (2021) 567–573.
[15] U. Zafar, et al., Assessing powder flowability at low stresses using ball indentation method: Evaluation of constraint factor, Powder Technol. 387 (2021) 287–294.
[16] Chuan Wang, Ali Hassanpour, Mojtaba Ghadiri, Characterisation of flowability of cohesive powders by testing small quantities of weak compacts, Particuology 6 (4) (2008) 282–285.
[17] Raymond C. Rowe, Paul J. Sheskey, Paul J. Weller (Eds.), Handbook of pharmaceutical excipients, Vol. 6, Pharmaceutical Press, London, 2006.
[18] Patrick Pan, et al., Hydroxypropyl methylcellulose bioadhesive hydrogels for topical application and sustained drug release: The effect of polyvinylpyrrolidone on the physicomechanical properties of hydrogel, Pharmaceutics 15 (9) (2023) 2360.
[19] Fuh-Shuenn Shyr, An approximate method to determine the surface tension from a sessile drop, J. Mater. Sci. Lett. 10 (16) (1991) 946–948.
[20] John H. Perry, Chemical engineers' handbook, 1950, p. 533.

[21] Walid F. Sakr, et al., Upgrading wet granulation monitoring from hand squeeze test to mixing torque rheometry, Saudi Pharm. J. 20 (1) (2012) 9–19.
[22] Toma Mihai Chitu, Driss Oulahna, Mehrdji Hemati, Rheology, granule growth and granule strength: Application to the wet granulation of lactose–MCC mixtures, Powder Technol. 208 (2) (2011) 441–453.
[23] Erica Franceschinis, et al., Prediction of the growth kinetics and agglomeration mechanisms using a mixer torque rheometer, Chem. Eng. Res. Des. 159 (2020) 328–338.
[24] GDR MiDi, On dense granular flows, Eur. Phys. J. E 14 (2004) 341–365.
[25] Frédéric Da Cruz, et al., Rheophysics of dense granular materials: Discrete simulation of plane shear flows, Phys. Rev. E—Stat. Nonlinear Soft Matter Phys. 72 (2) (2005) 021309.
[26] Ryan C. Hurley, José E. Andrade, Friction in inertial granular flows: competition between dilation and grain-scale dissipation rates, Granul. Matter 17 (3) (2015) 287–295.
[27] Melissa L. Sweat, Andrew S. Parker, Stephen P. Beaudoin, Compressive behavior of high-viscosity granular systems: Effects of viscosity and strain rate, Powder Technol. 302 (2016) 480–487.
[28] Melissa L. Sweat, Andrew S. Parker, Stephen P. Beaudoin, Compressive behavior of high viscosity granular systems: Effect of particle size distribution, Powder Technol. 311 (2017) 506–513.
[29] Monica Tirapelle, Andrea C. Santomaso, Colin Hare, Dynamic ball indentation for powder flow characterization, Powder Technol. 360 (2020) 1047–1054.
[30] M. Pasha, et al., Analysis of ball indentation on cohesive powder beds using distinct element modelling, Powder Technol. 233 (2013) 80–90.
[31] D.N. Mazzone, G.I. Tardos, R. Pfeffer, The behavior of liquid bridges between two relatively moving particles, Powder Technol. 51 (1) (1987) 71–83.
[32] Mustafa Güden, et al., Effects of compaction stress and particle shape on the porosity and compression mechanical properties of sintered Ti6Al4V powder compacts for hard tissue implantation, J. Biomed. Mater. Res. Part B: Appl. Biomater. 85 (2) (2008) 547–555.
[33] Karen P. Hapgood, James D. Litster, Rachel Smith, Nucleation regime map for liquid bound granules, AIChE J. 49 (2) (2003) 350–361.
[34] Umair Zafar, et al., Ball indentation on powder beds for assessing powder flowability: Analysis of operation window, Powder Technol. 310 (2017) 300–306.
[35] A. Santomaso, P. Lazzaro, Paolo Canu, Powder flowability and density ratios: the impact of granules packing, Chem. Eng. Sci. 58 (13) (2003) 2857–2874.